Dynamic multifunctional devices enabled by ultrathin metal nanocoatings with optical/photothermal and morphological versatility

Songshan Zeng[a,b], Zhuoran Yang[c], Zaili Hou[a,b], Cheonjin Park[d], Michael D. Jones[b], Hao Ding[a,b], Kuangyu Shen[a,b], Andrew T. Smith[a,b], Henry X. Jin[b], Bing Wang[d], Han Jiang[c,1], and Luyi Sun[a,b,e,1]

[a]Polymer Program, Institute of Materials Science, University of Connecticut, Storrs, CT 06269; [b]Department of Chemical and Biomolecular Engineering, University of Connecticut, Storrs, CT 06269; [c]School of Mechanics and Engineering, Southwest Jiaotong University, Chengdu, Sichuan 610031, China; [d]Department of Computer Science and Engineering, University of Connecticut, Storrs, CT 06269; and [e]Department of Biomedical Engineering, University of Connecticut, Storrs, CT 06269

Edited by David Weitz, Department of Physics, Division of Engineering and Applied Science, Harvard University, Cambridge, MA; received October 19, 2021; accepted December 13, 2021

Inspired by the intriguing adaptivity of natural life, such as squids and flowers, we propose a series of dynamic and responsive multifunctional devices based on multiscale structural design, which contain metal nanocoating layers overlaid with other micro-/nanoscale soft or rigid layers. Since the optical/photothermal properties of a metal nanocoating are thickness dependent, metal nanocoatings with different thicknesses were chosen to integrate with other structural design elements to achieve dynamic multistimuli responses. The resultant devices demonstrate 1) strain-regulated cracked and/or wrinkled topography with tunable light-scattering properties, 2) moisture/photothermal-responsive structural color coupled with wrinkled surface, and 3) mechanically controllable light-shielding properties attributed to the strain-dependent crack width of the nanocoating. These devices can adapt external stimuli, such as mechanical strain, moisture, light, and/or heat, into corresponding changes of optical signals, such as transparency, reflectance, and/or coloration. Therefore, these devices can be applied as multistimuli-responsive encryption devices, smart windows, moisture/photothermal-responsive dynamic optics, and smartphone app–assisted pressure-mapping sensors. All the devices exhibit high reversibility and rapid responsiveness. Thus, this hybrid system containing ultrathin metal nanocoatings holds a unique design flexibility and adaptivity and is promising for developing next-generation multifunctional devices with widespread application.

metal nanocoating | micro-/nanotopographies | smart material | multifunctional device | hybrid structure

Smart or stimuli-responsive materials have controllable optical, mechanical, electronic, and/or other properties that can be effectively converted by external stimuli, such as mechanical force (1–13), light (14–18), temperature (11, 18–20), moisture (17, 21–23), electricity (24–27), and so on (13, 27–30). One of the major efforts in this field is to mimic the intriguing micro-/nanotopographies of numerous organisms, which serve various functions in nature. For example, the dermal layer on the skin of *Cephalopods* (such as squid, octopus, cuttle fish, etc.) consists of microstructured radial muscles, which effectively modulate the exposure of the underlying chromatophores to dynamically change skin coloration for camouflage (3, 11, 22). Another vivid demonstration is the wrinkled surface, which can be created by imposing compression to a film-substrate bilayer with mismatched elastic modulus (31). These types of periodical micro-/nanotopographies possess unique light-scattering/diffraction/grating characteristics (16, 17, 21). Thus, wrinkle-like morphologies have been widely adopted on the petals of some flowers, such as *Hibiscus trionum* and *Tulipa* (32), to introduce vivid iridescent colors via diffraction gratings.

Analogous artificial micro-/nanotopographies, like cracks (3, 9, 11, 18), wrinkles (17, 21, 31), creases (27, 33), and grooves (34, 35), have been fabricated based on bilayer structures via the coupling of a rigid thin film and a soft substrate with strong interfacial bonding. Elastomers (such as polydimethylsiloxane [PDMS]) and hydrogels are the most common candidates used as the soft substrates (10, 16, 31), while the rigid thin film commonly consists of a polymer (10, 20, 21) or its composite with inorganic fillers (3, 36). However, there are several limitations in using these materials as thin films. Polymer-based films have low elastic moduli, especially compared with metals. Also, it is technically difficult to achieve uniform polymer films with a well-controlled thickness below 30 nm. These disadvantages severely restrain the fabrication of thin films in submicro-/nanoscale dimensions and limit the generation of corresponding micro-/nanomorphologies, which are essential to develop new morphology-driven multifunctional devices. For instance, when a polymer-based thin film is used in a bilayer system, it is hard to decrease the average intercrack spacing to <30 μm (3, 35,

Significance

Smart devices characterized by micro-/nanotopographies, such as cracks, wrinkles, folds, etc., have been fabricated for widespread application. Here, with the combination of multiscale hierarchical architecture, ultrathin metal nanocoatings with high optical/photothermal tunability and morphological versatility, and surface/interface engineering, a set of multifunctional devices with multistimuli responsiveness was fabricated. These devices can adapt to external stimuli with reversible and instantaneous responses in optical signals, which include strain-regulated light-scattering properties, photothermal-responsive wrinkled surface coupled with moisture-responsive structural color, and mechanically controllable light-shielding properties. The structural designs that rationally overlay micro-/nanostructured ultrathin nanocoatings with other elements are the key to realize this advanced system, which provides avenues for designing versatile, tunable, and adaptable multifunctional devices.

Author contributions: S.Z. and L.S. designed research; S.Z., Z.H., M.D.J., H.D., K.S., A.T.S., and H.X.J. performed research; S.Z., Z.Y., C.P., B.W., H.J., and L.S. contributed new reagents/analytic tools; S.Z., Z.Y., C.P., B.W., H.J., and L.S. analyzed data; and S.Z., Z.Y., H.J., and L.S. wrote the paper.

The authors declare no competing interest.

This article is a PNAS Direct Submission.

[1]To whom correspondence may be addressed. Email: jianghan@home.swjtu.edu.cn or luyi.sun@uconn.edu.

This article contains supporting information online at http://www.pnas.org/lookup/suppl/doi:10.1073/pnas.2118991119/-/DCSupplemental.

Published January 18, 2022.

36) or lower the wavelength of wrinkles to <3 μm (17, 21, 24, 37, 38), which typically requires a very low film thickness (<30 nm) to achieve such a low intercrack spacing and wrinkle wavelength. Also, in a polymer-based film system, it is very challenging to precisely tailor the optical reflectance, transmittance, and photothermal effect when the thin film is <30 nm in thickness.

In contrast, metal or metal alloy nanocoatings deposited by a simple but effective sputter-coating method demonstrate various advantages, including 1) precise control of the thickness of ultrathin and uniform nanocoatings within 30 nm via simply varying the sputter-coating condition and/or time (39); 2) much higher elastic modulus (~90 GPa) as compared with those of polymer films (~0.1 to 2 GPa); 3) highly tailorable reflectance, transmittance, and photothermal effect by modulating coating thickness (40, 41); 4) ease to fabricate macroscale predesigned patterns with the assistance of stencil masks; 5) omnidirectional sputter coating to simultaneously deposit coatings on multiple surfaces of the substrate; 6) a broad spectrum of metals and/or metal alloys can be applied as this rigid thin film; and 7) commercially available and highly accessible sputter coaters are promising for developing and scaling up these metal nanocoating-based devices. In addition, such sputter nanocoatings can achieve strong interfacial bonding with diverse soft substrates and rigid elements via covalent bonding (42–46) Thus, metal nanocoatings can be readily and seamlessly integrated into smart material systems as crucial micro-/nanostructured rigid thin-film layers.

Herein, we propose a series of multifunctional devices with multistimuli responsiveness, which contain metal nanocoatings as rigid thin films tightly bonded and laminated to other micro-/macroscale soft or rigid layers. Upon rationally optimizing the structural design of those elements, the resultant devices can demonstrate 1) strain-regulated cracked and/or wrinkled topographies with tunable light-scattering properties, 2) photothermal-responsive wrinkled surface coupled with moisture tailorable interference-induced structural color, and 3) mechanically controllable light-shielding properties attributed to the strain-dependent width of distributed cracks. This set of devices is able to adapt external stimuli, such as mechanical force, moisture, light, and/or heat, into the changes of optical signals, such as transparency, reflectance, and/or coloration. Therefore, they can be potentially applied as multistimuli-responsive encryption devices, smart windows, moisture/photothermal-responsive dynamic optics, and smartphone app–assisted pressure-mapping sensors. Also, all the devices exhibit remarkable reversibility and instantaneous responsiveness.

Results and Discussion

The sputter-coating schematic for depositing a metal nanocoating on an elastomeric substrate, using Au/Pd nanocoating (Au:Pd = 4:1, elastic modulus is ~89 GPa) and PDMS elastomeric substrate (elastic modulus ranging from 0.03 to 1.9 MPa) as examples, is shown in Fig. 1*A*. Sputter coating is a physical vapor deposition method that deposits a metal coating on a substrate with nanoscale thickness. The process begins with charging the coater by a high voltage (ca. 2 kV) to turn Ar gas into a plasma, which bombards the metal target and ejects metal atoms to subsequently and omnidirectionally deposit on a substrate (39). The representative topography of the Au/Pd film (using a 15.8-nm-thick Au/Pd coating as an example) demonstrated a flat surface as evident in the 5.8 μm^2 of atomic force microscope scan in Fig. 1*A*. Also, as shown in *SI Appendix*, Fig. S1, the resultant thickness of the Au/Pd coating can be easily and precisely modulated by varying the sputter-coating time with the target voltage, sputtering current, chamber pressure, and target-to-sample distance fixed (39).

The transmittance, reflectance in the visible light range, and photothermal performance as a function of metal nanocoating thickness in the Au/Pd–PDMS bilayer structures are shown in Fig. 1 *B–D*, respectively. As evident in Fig. 1*B*, the transmittances at the wavelength of 600 nm for the Au/Pd–PDMS bilayers with metal nanocoating thicknesses of 0, 6.5, 8.6, 11.9, 15.8, and 29.9 nm were 96.6, 92.8, 80.6, 44.4, 23.8, and 10.9%, respectively. Thus, the resultant bilayers demonstrated high transmittance close to that of pure PDMS (thickness of PDMS of ~1.1 mm) when the metal nanocoating thickness was <9 nm. As for the reflectance shown in Fig. 1*C*, the bilayers containing Au/Pd nanocoating with thicknesses of 0, 6.5, and 8.6 nm showed very close reflectance (at 600-nm wavelength) of 1.12, 1.35, and 1.79%, respectively. However, the bilayers containing Au/Pd nanocoating with thicknesses of 11.9, 15.8, and 29.9 nm had higher reflectance (at 600-nm wavelength) of 12.6, 19.5, and 25.9%, respectively. Thus, similar trends were also evidently shown in the digital photo in Fig. 1*B*. To evaluate the photothermal performance, the bilayers containing a metal nanocoating with thicknesses of 0, 15.8, and 29.9 nm were irradiated under a Xeon lamp (power = 300 W) with a distance of 10 cm, as shown in Fig. 1*D*. It is clear that the bilayer with a 15.8-nm nanocoating exhibited a temperature of 79.4 °C after 3 min of illumination, which was much higher than the temperature (56.1 °C) of the pure PDMS without a metal nanocoating.

Since the thickness of Au/Pd coating on PDMS can significantly influence the resultant light transmittance, reflectance, and photothermal performance, three types of structural designs with different Au/Pd thicknesses were conducted to fabricate different function-orientated devices. As illustrated in Fig. 1*E*, when a layer of Au/Pd nanocoating with a thickness <9 nm was deposited atop PDMS, stretching this Au/Pd–PDMS structure can generate a strain-regulated cracked and wrinkled topography, which can induce tunable light-scattering properties to modulate macroscale transmittance and reflectance. Thus, a mechanically revealable encryption device and a highly strain-responsive smart window can be achieved based on this design strategy. If the Au/Pd nanocoating thickness is increased to ca. 15.8 nm, the light reflectance and photothermal effect can be significantly intensified. This permits a polyvinyl alcohol (PVA)–Au/Pd–PDMS triple-layered structure to exhibit moisture-responsive interference-induced structural color and a laser rewritable wrinkled surface attributed to the photothermal effect (Fig. 1*E*). Upon further enhancing the Au/Pd thickness to ca. 29.9 nm, the metal coating has an effective light-shielding characteristic that allows the metal coating to act as a "shutter" to dynamically modulate the exposed area of an underlying substrate, resulting in the fabrication of various multistimuli-responsive devices with mechanochromic response. Notably, the aforenoted devices all require strong interfacial bonding between the metal coating and the PDMS. Previous investigations have demonstrated that a (3-mercaptopropyl) trimethoxysilane (MPTMS)–treated Au coating can bond to PDMS by casting the PDMS precursor prior to thermal curing (45, 46). Also, it was reported that the Au coating can bond to the MPTMS-modified PDMS surface (45). Thus, in this work, an ultrafast flame activation treatment (for achieving a thinner activated layer) or an ultraviolet ozone (UVO) treatment (for achieving a thicker activated layer) was applied to turn the C–H bonds on the PDMS surface into alkyl radicals, which can react with oxygen in the ambient environment to generate new hydrophilic sites with silanol groups (42, 47). The MPTMS treatment was then applied to the activated PDMS surface, which can realize strong bonding to the Au/Pd coating (*SI Appendix*, Fig. S2) (42, 43).

As shown in Fig. 2*A* and Movie S1, for the mechanically revealable encryption device, the "C" macroscale pattern with a 6.5-nm Au/Pd coating is well concealed and invisible to the

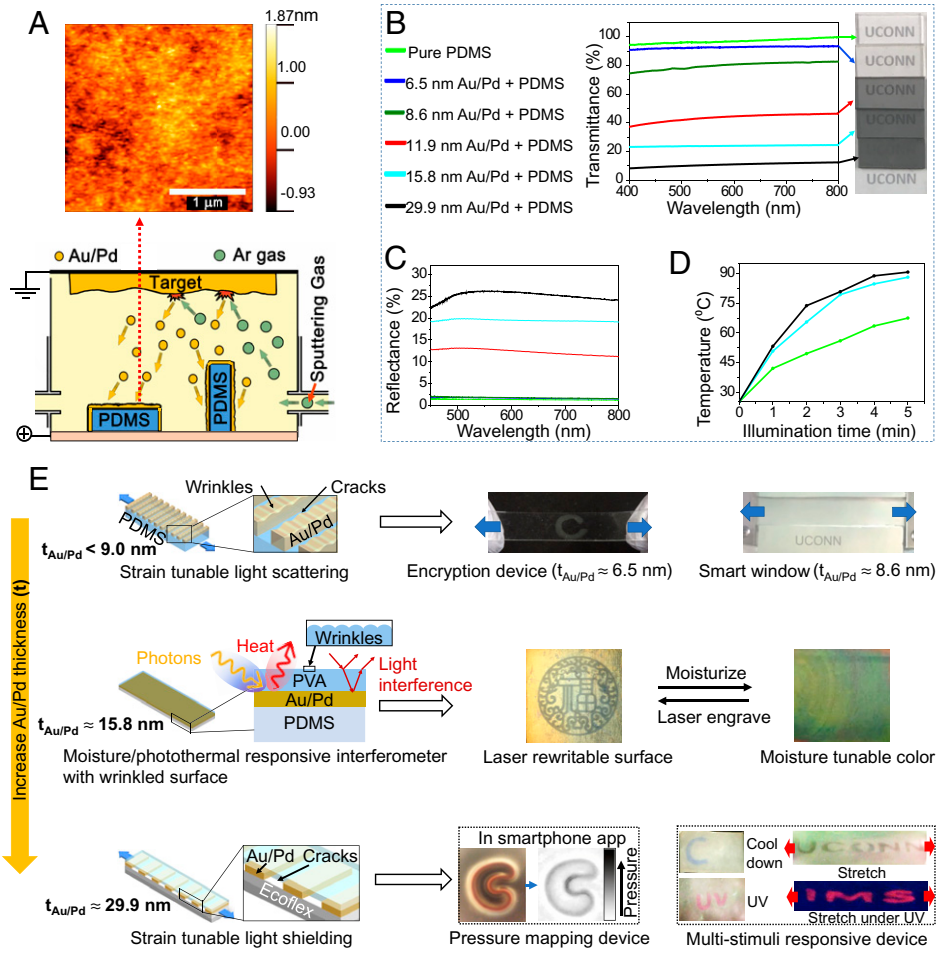

Fig. 1. Characterizations of the Au/Pd nanocoatings and schematics of the designed devices. (*A*) Atomic force microscopic image of the Au/Pd nanocoating deposited on a PDMS surface and schematic of the sputter-coating process. (*B*) Light transmittance, (*C*) reflectance, and (*D*) photothermal performance of the Au/Pd–PDMS bilayer structures with different thicknesses of metal nanocoatings. (*E*) Design schematic of the three types of dynamic stimuli-responsive devices.

naked eye due to its surface reflectance being close to that of pure PDMS. Stretching the device can induce longitudinal cracks perpendicular to the stretching direction and horizonal-oriented wrinkles (wavelength of wrinkles = 1.8 μm) due to the Poisson effect on the C macroscale patterned area covered by the Au/Pd nanocoating, which changes the topography to significantly alter the light-scattering properties. As shown in Fig. 2*B*, the transmittance at the wavelength of 600 nm on the C macroscale patterned area changed from 90.1% at 0% stretching strain to 43.2% at 30% strain, whereas the corresponding reflectance at the wavelength of 600 nm at the same spot changed from 1.6% at 0% strain to 0.1% at 30.0% strain. Also, the wrinkle amplitude and the corresponding surface roughness average (Ra) on the C macroscale patterned area raised to 0.38 and 0.23 μm at 30.0% stretching strain, respectively (*SI Appendix*, Fig. S3). Thus, the mechanically responsive surface topographies and optical properties allow the originally concealed C macroscale pattern to become visible under stretching and concealed as released.

Also, these strain-tunable wrinkled and cracked topographies can be further exploited for the application of smart windows, which can be achieved by depositing an 8.6-nm-thick Au/Pd nanocoating on both sides of the treated PDMS (denoted as Au/Pd–PDMS–Au/Pd). The resultant topographies on both sides of the device exhibited analogous strain dependence from flat surface to a rough surface characterized with longitudinal open cracks and horizontal wrinkles at 25.0% strain. Herein, the Ra of the device at 25.0% strain increased to 0.27 μm (*SI Appendix*, Fig. S4), and the corresponding wrinkles demonstrated a wavelength of ca. 2.1 μm and an amplitude of ca. 0.36 μm (Fig. 2*C*). This characteristic enables the device to display reversible and highly sensitive strain-dependent transmittance for smart window application. As shown in Fig. 2*C*, the "UCONN" logo background was originally visible through the device at a released state. Upon stretching to 25.0% strain, the logo became obscured, which can be attributed to the formation of mechanical-responsive micro-/nanotopographies, especially wrinkles, that dramatically changed the light-scattering properties (Movie S2) (24, 48). Fig. 2*D* shows that the corresponding transmittance at the wavelength of 600 nm was 79.1% at 0% stretching strain, and then, the value decreased to 50.1% at 9.3% strain, to 38.3% at 14.0% strain, and to 26.1% at 23.3% strain, featuring an optical transmittance modulation range of 53.0% within 23.3% stretching strain. Another control sample, which had the same 8.6-nm Au/Pd nanocoating but only deposited on one side of PDMS substrate, was also fabricated. As shown in *SI Appendix*, Fig. S5*A*, the control sample exhibited a similar initial transmittance at the wavelength of 600 nm of 80.6% at 0% stretching strain. However, it only dropped to 63.6% at 11.4% strain and to 53.8% at 25.7% strain, respectively, demonstrating a much lower optical transmittance modulation range of 26.8% within 25.7%

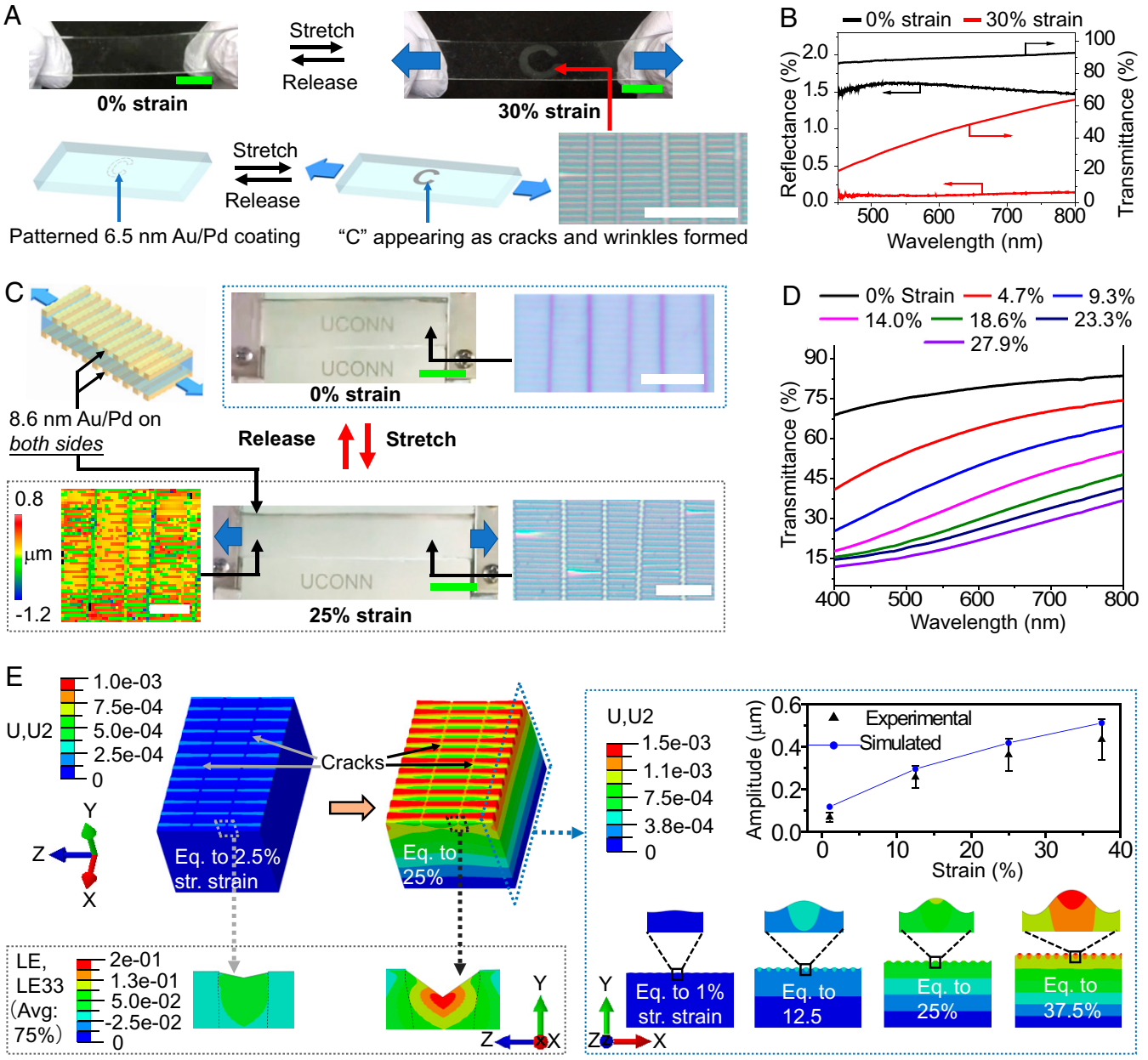

Fig. 2. Characterizations and performance of the devices based on the Au/Pd–PDMS or Au/Pd–PDMS–Au/Pd-layered structure. (*A*) Characterizations and performance of the mechanically revealable encryption device. (Scale bars: white, 25 μm; green, 1 cm.) (*B*) Strain-dependent transmittance and reflectance of the mechanically revealable encryption device. (*C*) Schematic, characterizations, and performance of the smart window device. (Scale bars: white, 25 μm; green, 1 cm.) (*D*) Strain-responsive transmittance of the smart window device. (*E*) FE wrinkling simulation equivalent to those wrinkling under different stretching strains in the experiment for the smart window device shown in *C* (error bars are defined as SDs; str.: stretching).

stretching strain as compared with that of Au/Pd–PDMS–Au/Pd (*SI Appendix*, Fig. S5 *B* and *C*). Notably, this triple-layered system also demonstrates a good reversibility by showing consistent strain-responsive optical modulation before and after the cyclic test (0 to 35.0% strain, 1,000 cycles) (*SI Appendix*, Fig. S6), which can be attributed to the strong covalent bonding between the Au/Pd nanocoating and PDMS as well as the excellent elasticity and shape recovery of PDMS substrate within the stretching strain range (<40% strain) (49, 50). As shown in Fig. 2*E*, finite element (FE) simulations for the wrinkle formations under the different stretching strains were conducted by using the Abaqus software (version 2020) based on previous work (51–53). The simulation details can be found in *SI Appendix*, Fig. S7, *SI Text*, and Table S1. The FE-simulated wrinkle amplitudes are consistent with the experimental values. Since the wrinkle formation is triggered by the compression strain perpendicular to the tensile stretch direction due to the Poisson effect, with an increasing strain, the wrinkle amplitude increased significantly, reaching up to ca. 40 times the film thickness at a stretching strain of 25.0%.

Since the 15.8-nm-thick Au/Pd nanocoating exhibited a decent photothermal effect and a strong reflectance of 19.5% at the wavelength of 600 nm, by combining this nanocoating with a moisture-sensitive polymer PVA and an elastic substrate PDMS, it can be used as a crucial reflective and photothermal layer to achieve a moisture/photothermal-responsive interferometer with a wrinkled surface (Fig. 3*A*). The device is made of an Au/Pd coating sandwiched by a PVA layer on the top and a

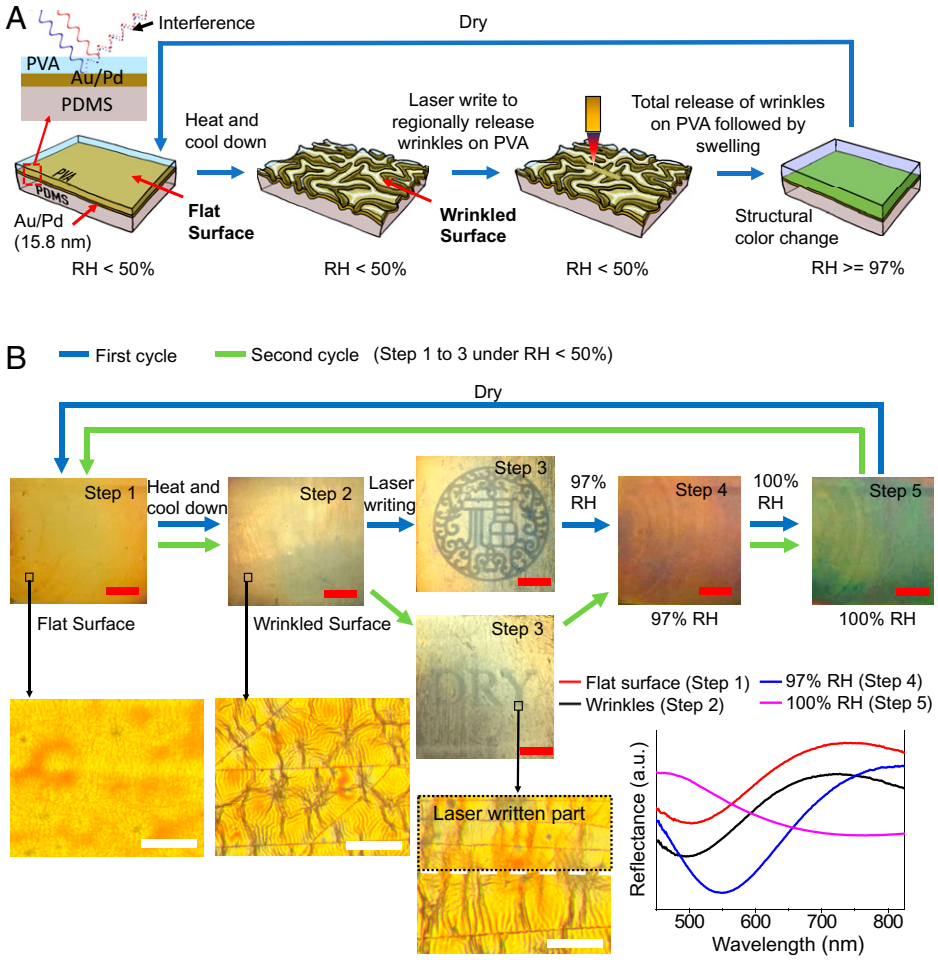

Fig. 3. Characterizations and performance of the device based on the PVA–Au/Pd–PDMS triple-layered structure. (*A*) Fabrication and response schematic of the moisture/photothermal-responsive interferometer with a wrinkled surface based on the PVA–Au/Pd–PDMS triple-layered structure. (*B*) Performance and characterizations of the PVA–Au/Pd–PDMS triple-layered structure. (Scale bars: white, 100 μm; red, 0.5 cm.)

PDMS layer as a bottom substrate (denoted as PVA–Au/Pd–PDMS) (*SI Appendix*, Fig. S8 shows the fabrication steps). As shown in Fig. 3*A*, this unique structure enables the creation of a yellow structural color that originated from the interference of the light beams reflected from the PVA–air interface and the Au/Pd–PVA interface (29, 54, 55). Additionally, since this structure is composed of thin film and substrate with mismatched thermal expansion coefficient, microscale wrinkles can be generated after the device is under heating prior to cooldown (56). Also, as shown in Fig. 3*A*, a laser engraver (0.6 W) can regionally release the formed wrinkles on the PVA layer. That is because the photothermal effect of the Au/Pd layer can create sufficient heat to regionally release the internal stress on the PVA film. Note that the wrinkles formed on a control sample containing only a PVA and PDMS bilayer without an Au/Pd layer cannot be released by the laser beam under the same power due to the lack of sufficiently high photothermal effect (the optical microscopic images are shown in *SI Appendix*, Fig. S9). This laser responsiveness permits customizable patterns to be written on wrinkled surface. The PVA (Kuraray POVAL^{TM} 8-88) used in this work has a molecular weight of ca. 67,000 and a degree of hydrolysis of 88%. Here, the application of PVA with a low degree of hydrolysis makes the film highly sensitive to moisture (17, 24). Thereafter, the remaining wrinkles on the PVA film can be completely erased by moisture as the internal stress of the highly hydrophilic PVA molecular chains can be released by moisture. Additionally, this moisturization process at a high humidity (≥97% relative humidity [RH]) will also increase the thickness of the PVA film due to the swelling effect, which can change the corresponding interference-induced structural color (29, 54). The corresponding stimuli-responsive performance of the device is shown in Fig. 3*B*. At step 1 of the first cycle, the device with an originally flat surface exhibited a yellow structural color. At step 2, a wrinkled surface with a very similar structural color can be formed on the PVA film upon heating to 80 °C followed by cooling down to room temperature. At step 3, a laser engraver was subsequently applied to regionally release the wrinkles to make a customizable pattern (steps 1 to 3 remaining at <50% RH). At step 4, upon exposure to a high RH of 97%, the wrinkles on the PVA film were erased, leading to the disappearance of the pattern, concomitant with the structural color changing from yellow to red–orange. Additionally, the structural color can be further converted to green at 100% RH at step 5, which can be returned to yellow upon drying, identical to the color shown in step 1. The corresponding reflectance spectra for steps 1, 2, 4, and 5 are shown in Fig. 3*B*. To quantitatively analyze the laser- or moisture-induced wrinkle release shown in Fig. 3, the Ra during these treatment processes is presented in *SI Appendix*, Fig. S10. Herein, the wrinkled area has an Ra value of 0.160 μm, while the Ra of the laser-engraved area dropped to 0.022 μm, demonstrating the release of the wrinkles. After exposing the whole surface to moisture at a high humidity (≥97% RH) prior to drying, all the wrinkles were released, and the topography

turned into a flat surface with a low Ra of 0.017 μm. Notably, a second cycle from step 1 to step 5 in Fig. 3 with a different macroscale pattern of "DRY" was also presented, demonstrating that the laser can reversibly write macroscale patterns on the wrinkled PVA surface and the macroscale patterns can be completely erased by moisture (pattern resolution is ca. 100 μm based on the technical limitation of the engraver).

As the Au/Pd coating with a thickness of 29.9 nm presents remarkable light-shielding properties, it can be used to prepare mechanochromic devices with strain-regulated distributed cracks. As shown in Fig. 4*A*, this multilayered mechanochromic device consists of a thin hard PDMS (modulus ~1.9 MPa, thickness ~0.27 mm) and a thick soft PDMS (modulus ~30 kPa, thickness ~6.38 mm) atop a layered structure composed of a 29.9-nm-thick Au/Pd coating sandwiched by two Ecoflex elastomeric protective layers (modulus ~30 kPa, thickness ~0.27 mm), which are all on the top of a red color Ecoflex/red dye substrate (modulus ~30 kPa, thickness ~1.23 mm). A pre-stretching process was conducted to generate uniform and densely distributed cracks (*Materials and Methods*). At a released state, the underlying red color substrate was well shielded by the Au/Pd layer with the distributed cracks closed. Thus, the device displayed a yellow–gray color of the Au/Pd layer (Fig. 4*B*). Upon stretching, the cracks on the Au/Pd layer started to open, exposing the underlying substrate. Thus, as evident in Fig. 4*B*, the color of the device converted into a

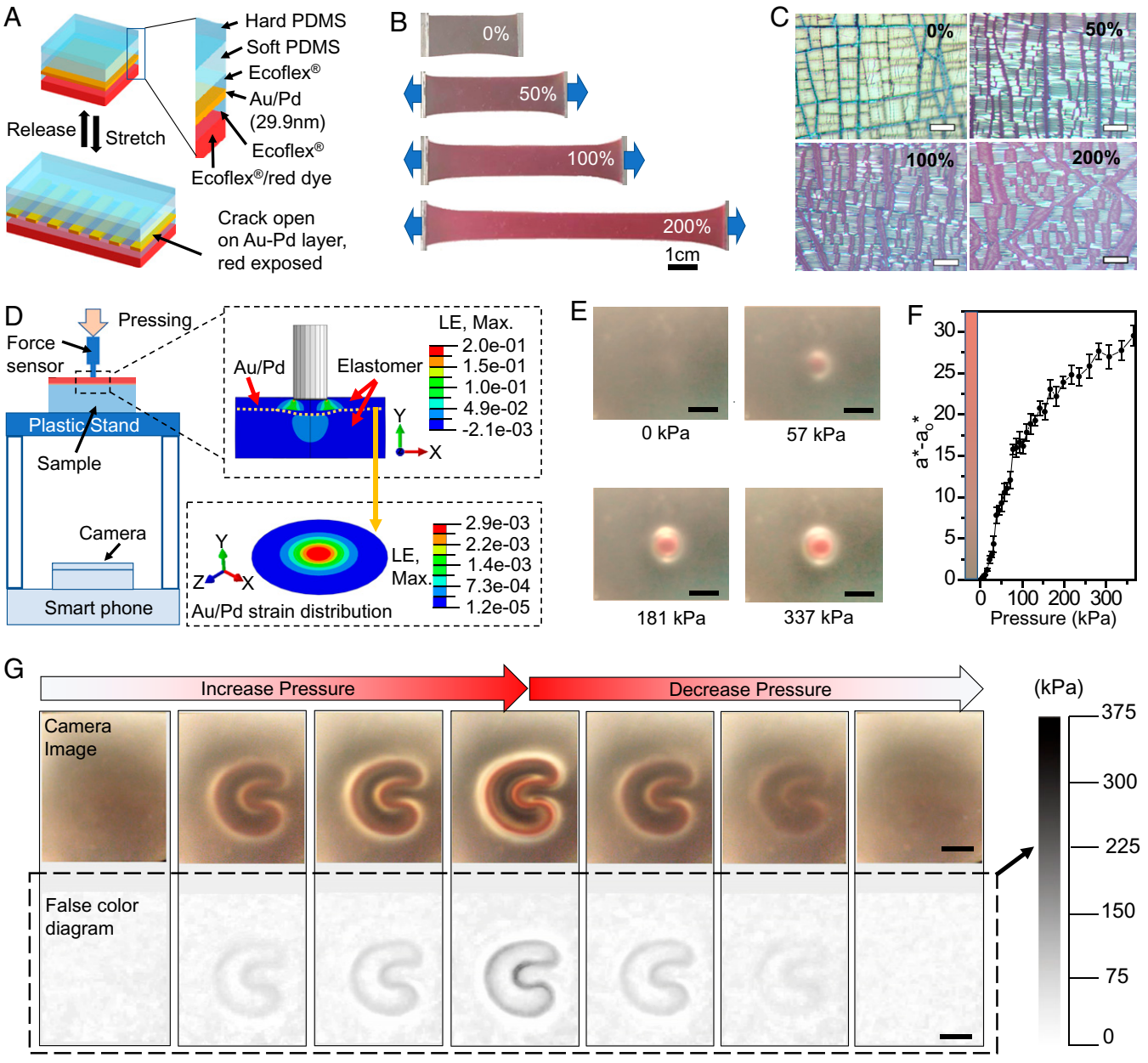

Fig. 4. Characterizations and performance of the devices with mechanically controllable light-shielding effect. (*A*) Design schematic of the mechanochromic device. (*B*) Performance of the mechanochromic device under stretching. (*C*) optical microscopic images of cracking topographies on the Au/Pd nanocoating atop the red color Ecoflex/red dye substrate as a function of stretching strain. (Scale bars: 100 μm.) (*D*) Schematic of the smartphone app–assisted pressure-mapping sensor and the corresponding FE simulation result under indentation. (*E*) Performance of the smartphone app–assisted pressure-mapping sensor. (Scale bars: 1 cm.) (*F*) The a*-value change of the La*b* color coordinates of the pressure-mapping sensor as a function of pressure (error bars are defined as SDs). (*G*) Performance of the smartphone-assisted pressure-mapping sensor. (Scale bars: 1 cm.)

noticeable red at a strain of 50%, and the degree of red was further intensified upon stretching to a strain >100%. The corresponding changes of a* values in the Commission Internationale de l'Elcairage (CIE) La*b* color coordinates increased from 3.2 at 0% strain to 14.5 at 50% strain, 24.8 at 100% strain, and 33.4 at 200% strain (*SI Appendix*, Fig. S11). Here, the CIE La*b* is a color space interpreting visible colors via the combination of L (lightness), a* channel (describing the changing degree from green to red), and b* channel (describing the changing degree from blue to yellow). Thus, a larger a* value indicates a higher degree of red color. Fig. 4*C* shows the corresponding strain-dependent cracking topographies on the Au/Pd nanocoating atop the red color Ecoflex/red dye substrate, which exhibited an increasing exposed area of the underlying substrate with stretching strain due to the enlarged crack opening width that increased to 10.1 μm at 50% strain, to 25.9 μm at 100% strain, and to 61.2 μm at 200% strain (*SI Appendix*, Fig. S12).

This mechanochromic device shown in Fig. 4*A* can be further applied as a low-cost smartphone app–assisted pressure-mapping sensor. As shown in Fig. 4*D*, the Ecoflex/red dye substrate was placed toward an indenting object, while the PDMS side faced a transparent plastic stand that was placed above a smartphone camera. As the sample subject to indentation/pressing, the corresponding FE-simulated strain distribution on the pressure-mapping sensor is shown in Fig. 4*D* (*SI Appendix*, Fig. S13, *SI Text*, and Table S2 have simulation details). Although the main deformation of the indented sensor occurs above the Au/Pd coating in the direction of the *y* axis due to the large elastic modulus of this metal layer, a significant tensile strain on the Au/Pd coating can also be observed below the indenter. Thus, the FE analysis suggests that the tensile strain on the Au/Pd coating resulted from the indentation/pressing process would lead to an expansion of the crack width with concomitant macroscale color changes. As shown in Fig. 4*E*, upon pressing the pressure-mapping sensor with a circular-shaped intender, the pressed area became increasingly red, with the pressure being enhanced to 57, 181, and 337 kPa. The corresponding red color variation was interpreted by the a*-value change on the central part of this circular shape as a function of pressure (Fig. 4*F*). Thus, the average $a^*–a_o^*$ value progressively increased from 15.3 at 102 kPa to 23.1 at 198 kPa and to 26.1 at 308 kPa. Here, a_o^* is the a* value on the central part when the pressure is 0 kPa. Note that this curve enables to match between the a*-value change and the corresponding indenting pressure. Thus, a corresponding smartphone app was developed, which can convert the pressure-induced color change captured by a camera into a corresponding black and white false color diagram indicating the real-time pressure mapping ranging from 0 to 375 kPa (Fig. 4*G* and Movie S3).

The 29.9-nm-thick Au/Pd nanocoating can also be applied in fabricating an encryption device with multistimuli-responsive revealable patterns. In this device, four types of concealed patterns with different colors can be revealed by applying four different stimuli, including alerting temperature (cooling), ultraviolet (UV) light at 365 nm under visible light, stretching under visible light, and stretching under UV light at 254 nm in a dark environment (*SI Appendix* has preparation steps). As shown in Fig. 5, to realize this multistimuli-responsive patterning system, thermochromic/photochromic patterns encapsulated by Ecoflex were assembled side by side atop an Ecoflex-encapsulated TiO_2 (enabled white color appearance) and Au/Pd light-shielding layer. The C pattern made by a thermochromic pigment has a white color at room temperature but turns to blue when cooled down below 15 °C, whereas the "UV" pattern made by a photochromic pigment also has a white color under visible light but changes to pink–red when exposed to UV light at 365 nm (*SI Appendix*, Fig. S14 shows the performances of the pigments).

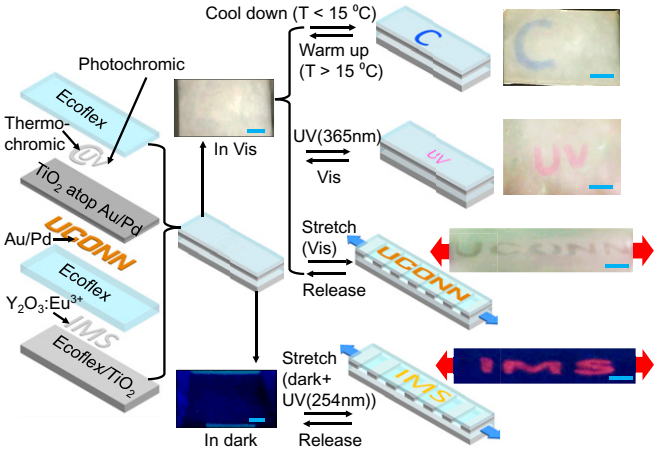

Fig. 5. Design schematic of the multistimuli-responsive encryption device with four concealed patterns revealed under different stimuli. Vis: visible light. (Scale bars: 1 cm.)

Thus, these two patterns are invisible at room temperature under visible light as both pigments and light-shielding layers are white color under this condition; they can only be revealed upon being cooled down to <15 °C and exposed to UV light at 365 nm, respectively. Under the light-shielding layer, there is a sputter-coated UCONN Au/Pd pattern atop a pure Ecoflex layer. The macroscale pattern is only visible under a stretching condition under visible light due to the crack opening of the light-shielding layer. Under the UCONN pattern and the Ecoflex layer, there is a layer of "IMS"-patterned Y_2O_3:Eu^{3+} atop a white Ecoflex/TiO_2 bottom substrate. Since both Y_2O_3:Eu^{3+} powders and the substrate layer are white under visible light, the IMS pattern is invisible if stretched under this condition. Upon stretching the sample under UV light at 254 nm and a dark environment, the strong fluorescence of Y_2O_3:Eu^{3+} can be activated, and the IMS pattern becomes visible due to the opening of the cracks on the light-shielding layer. Thus, by taking advantage of this three-dimensional integration strategy, we realized an encryption device that can reveal four different concealed patterns by four individual stimuli (Movie S4).

Conclusion

In summary, the Au/Pd nanocoating used in this work possesses various advantages: precise control of thickness within 30 nm; high elastic modulus; highly tunable transmittance, reflectance, and photothermal effect via modulating thickness; ease of patterning; omnidirectional coating nature; high reversibility; strong interfacial bonding to other layers; versatility of metal selection; and promising potential for production. Herein, nanocoatings with different thicknesses were chosen to integrate with other soft/hard structural design elements to achieve dynamic multistimuli-responsive systems. For instance, nanocoatings with thicknesses of 6.5 and 8.6 nm were chosen to deposit on one/both sides of a PDMS substrate, leading to devices that can reversibly convert between a flattened surface and a cracked/wrinkled surface concomitant with the change of light-scattering properties via applying mechanical strain. Therefore, a mechanically revealable encryption device was designed that can reversibly reveal/conceal customizable patterns. Additionally, a strain-responsive smart window was also fabricated, which demonstrated an excellent optical modulation of 53.0% in transmittance (at 600-nm wavelength) within 23.3% strain. If the thickness of the nanocoating was further increased to 15.8 nm, the corresponding reflectance and photothermal effect can be significantly enhanced. Upon sandwiching

this nanocoating in between a PVA film and a PDMS substrate, a moisture/photothermal-responsive interferometer with a wrinkled surface was prepared, which can demonstrate moisture-responsive structural color and features with a laser-rewritable wrinkled surface. As the thickness of the nanocoating was increased up to 29.9 nm, the resultant nanocoating possesses remarkable strain-responsive light-shielding effect, which permits us to tune the exposure of underlying substrate via mechanical strain. Thus, a low-cost smartphone-assisted pressure-mapping sensor was invented, which can sense pressures between 0 and 375 kPa via a smartphone app. Moreover, a multistimuli-responsive encryption device with four concealed patterns can be revealed by cooling, UV light, or stretching under different environments. All the aforenoted devices present high reversibility and durability. Since the metal nanocoating itself used in this work is electrically conductive, it can be further explored as a piezoresistive device in combination with the mechanochromic behavior. Thereafter, this system can be explored for strain-sensing applications integrating electrical and optical signals in the future. Overall, these ultrathin metal nanocoatings generated by a commercial sputter coater hold unique design flexibility, adaptivity, and advantages. They act as crucial micro-/nanostructured layers to overlay with other elements for the multiscale structural design of next-generation multifunctional devices with widespread application.

Materials and Methods

Preparation of the Mechanically Revealable Encryption Device and the Strain-Responsive Smart Window. A stencil mask was placed atop a polystyrene (PS) petri dish foundation (diameter = 85 mm; from Fisher Scientific) followed by sputter coating a layer of 6.5-nm-thick Au/Pd (sputter-coater model: Polaron E5100 sputter-coating system) with subsequent MPTMS vapor treatment. After the stencil mask was removed, a liquid PDMS precursor (base to curing agent ratio = 20:1) was then cast atop the MPTMS-treated Au/Pd pattern followed by thermal curing at 80 °C for 2 h; it was subsequently peeled off from the foundation in one direction and cut into dimensions of 65 × 11 × 1.1 mm. To generate denser and more uniform crack distribution on the Au/Pd coating, the bilayer was prestretched to 40% uniaxial strain in the length direction prior to releasing back to 0% strain.

Preparation of the Strain-Responsive Smart Window. A PDMS strip (base to curing agent ratio = 20:1, cured at 80 °C for 2 h) with dimensions of 65 × 11 × 1.1 mm was prepared. To achieve a thin activated layer, both surfaces of the sample were then uniformly treated by flame activation using a piezo ignition jet torch (model: Master Appliance MT-51 Butane Micro Torch) at a distance of 1.5 cm and a duration of 2 s prior to an MPTMS vapor treatment. Subsequently, an 8.6-nm-thick Au/Pd layer was simultaneously sputter coated on both surfaces of the sample. The resultant sample was prestretched to 40% uniaxial strain in the length direction and then released to create denser and more uniform crack distribution.

Preparation of the Moisture/Photothermal-Responsive Interferometer with a Wrinkled Surface. A PVA film with a thickness of 420 nm was cast on a PS petri dish prior to an MPTMS vapor treatment. A layer of Au/Pd with a thickness of 15.8 nm was then sputter coated atop the PVA layer followed by another MPTMS vapor treatment, casting a layer of PDMS (thickness = 1.2 mm, base to curing agent ratio = 20:1), and curing at 80 °C for 2 h. The sample was then carefully peeled off from the foundation in one direction. Subsequently, the sample was placed in an oven at 80 °C for 20 min followed by cooling down to room temperature to form a wrinkled surface on the PVA film. A laser-engraving machine (model: NiocTech 3000 mW, laser power = 0.6 W) was applied to create customized patterns on the PVA film.

Preparation of the Pressure-Mapping Mechanochromic Sensor. A 1.23-mm Ecoflex 00-30/red dye/white dye layer (weight ratio = 400:8:7) was cast atop a PS petri dish foundation (diameter = 85 mm; from Fisher Scientific) prior to curing at 80 °C for 2 h. A layer of pure Ecoflex 00-30 with a thickness of 0.27 mm was then cast atop the above-mentioned layer followed by curing at 80 °C for 2 h. The Ecoflex surface was then exposed to a 20-min UVO irradiation in a Novascan PSD digital UVO system followed by an MPTMS vapor treatment. A nanocoating of Au/Pd with a thickness of 29.9 nm was then deposited atop the Ecoflex layer prior to another MPTMS vapor treatment. Subsequently, a layer of soft PDMS (base to curing agent ratio = 65:1, thickness = 6.38 mm) was cast atop the Au/Pd coating followed by curing at 80 °C for 2 h. A layer of harder PDMS (base to curing agent ratio = 10:1, thickness = 0.27 mm) was then cast atop the soft PDMS followed by curing at 80 °C for 2 h. The sample was then peeled off from the foundation in one direction. The peeling process induced distributed cracks on the metal nanocoating perpendicular to the peeling direction due to the brittle nature of the Au/Pd layer. To generate denser and more uniform crack distribution on the metal coating, a biaxial prestretching strain (60% on each direction) was then conducted (one stretching direction being the peeling direction) prior to releasing back to 0% strain.

Data Availability. All data that support this study are included in the article and/or supporting information.

ACKNOWLEDGMENTS. A.T.S. acknowledges Graduate Assistance in Areas of National Need Fellowship P200A150330.

1. G. Isapour, M. Lattuada, Bioinspired stimuli-responsive color-changing systems. *Adv. Mater.* **30**, e1707069 (2018).
2. J. Wang *et al.*, All-optical reversible azo-based wrinkling patterns with high aspect ratio and polarization-independent orientation for light-responsive soft photonics. *ACS Appl. Mater. Interfaces* **11**, 25595–25604 (2019).
3. S. Zeng *et al.*, Bio-inspired sensitive and reversible mechanochromisms via strain-dependent cracks and folds. *Nat. Commun.* **7**, 11802 (2016).
4. C. Wu *et al.*, Efficient mechanoluminescent elastomers for dual-responsive anticounterfeiting device and stretching/strain sensor with multimode sensibility. *Adv. Funct. Mater.* **28**, 1803168 (2018).
5. S. Chen *et al.*, Transparent and waterproof ionic liquid-based fibers for highly durable multifunctional sensors and strain-insensitive stretchable conductors. *ACS Appl. Mater. Interfaces* **10**, 4305–4314 (2018).
6. Z. Ma *et al.*, Mechanics-induced triple-mode anticounterfeiting and moving tactile sensing by simultaneously utilizing instantaneous and persistent mechanoluminescence. *Mater. Horiz.* **6**, 2003–2008 (2019).
7. Y. Jiang *et al.*, Dynamic optics with transparency and color changes under ambient conditions. *Polymers (Basel)* **11**, 103 (2019).
8. S. Chen *et al.*, A biomimetic interface with high adhesion, tailorable modulus for on-skin sensors, and low-power actuators. *Chem. Mater.* **31**, 8708–8716 (2019).
9. Z. Mao *et al.*, Dynamic mechanochromic optics with tunable strain sensitivity for strain-responsive digit display. *Adv. Opt. Mater.* **8**, 2001472 (2020).
10. Y. Xu *et al.*, Transparency change mechanochromism based on a robust PDMS-hydrogel bilayer structure. *Macromol. Rapid Commun.* **42**, e2000446 (2021).
11. S. Zeng *et al.*, Dynamic thermal radiation modulators via mechanically tunable surface emissivity. *Mater. Today* **45**, 44–53 (2021).
12. M. Hu *et al.*, High-performance strain sensors based on bilayer carbon black/PDMS hybrids. *Adv. Compos. Hybrid Mater.* **4**, 514–520 (2021).
13. B. Tian *et al.*, Stress-induced color manipulation of mechanoluminescent elastomer for visualized mechanics sensing. *Nano Energy* **83**, 105860 (2021).
14. B. Yang, F. Cai, S. Huang, H. Yu, Athermal and soft multi-nanopatterning of azopolymers: Phototunable mechanical properties. *Angew. Chem. Int. Ed. Engl.* **59**, 4035–4042 (2020).
15. P. Zhang, F. Cai, W. Wang, G. Wang, H. Yu, Light-switchable adhesion of azobenzene-containing siloxane-based tough adhesive. *ACS Appl. Polym. Mater.* **3**, 2325–2329 (2021).
16. H. Hou, J. Yin, X. Jiang, Smart patterned surface with dynamic wrinkles. *Acc. Chem. Res.* **52**, 1025–1035 (2019).
17. S. Zeng *et al.*, Smart laser-writable micropatterns with multiscale photo/moisture reconstructible structure. *Adv. Funct. Mater.* **31**, 2009481 (2021).
18. S. Zeng *et al.*, Multi-stimuli responsive chromism with tailorable mechanochromic sensitivity for versatile interactive sensing under ambient conditions. *Mater. Horiz.* **7**, 164–172 (2020).
19. A. T. Smith *et al.*, Multi-color reversible photochromisms via tunable light-dependent responses. *Matter* **2**, 680–696 (2020).
20. S. Zeng *et al.*, Spontaneous formation of wrinkle-driven tubular structure as a versatile platform for adaptive 3D stretchable electronics. *Mater. Horiz.* **7**, 2368–2377 (2020).
21. S. Zeng *et al.*, Moisture-responsive wrinkling surfaces with tunable dynamics. *Adv. Mater.* **29**, 1700828 (2017).
22. R. T. Hanlon *et al.*, Cephalopod dynamic camouflage: Bridging the continuum between background matching and disruptive coloration. *Philos. Trans. R. Soc. Lond. B Biol. Sci.* **364**, 429–437 (2009).
23. W. Hu *et al.*, Humidity-responsive blue phase liquid-crystalline film with reconfigurable and tailored visual signals. *Adv. Funct. Mater.* **30**, 2004610 (2020).
24. S. Zeng *et al.*, Tailoring multistimuli responsive micropatterns activated by various mechanical modes. *Adv. Funct. Mater.* **31**, 2100612 (2021).

25. C. Xu, G. T. Stiubianu, A. A. Gorodetsky, Adaptive infrared-reflecting systems inspired by cephalopods. *Science* **359**, 1495–1500 (2018).
26. C. Xu, M. Colorado Escobar, A. A. Gorodetsky, Stretchable cephalopod-inspired multimodal camouflage systems. *Adv. Mater.* **32**, e1905717 (2020).
27. Q. Wang, M. Tahir, J. Zang, X. Zhao, Dynamic electrostatic lithography: Multiscale on-demand patterning on large-area curved surfaces. *Adv. Mater.* **24**, 1947–1951 (2012).
28. X. Yu, Z. Wang, Y. Jiang, F. Shi, X. Zhang, Reversible pH-responsive surface: From superhydrophobicity to superhydrophilicity. *Adv. Mater.* **17**, 1289–1293 (2005).
29. M. Sun *et al.*, Hydrogel interferometry for ultrasensitive and highly selective chemical detection. *Adv. Mater.* **30**, e1804916 (2018).
30. L. Jia *et al.*, Leather based multi-stimuli responsive chromisms. *Adv. Funct. Mater.* **31**, 2104427 (2021).
31. S. Yang, K. Khare, P.-C. Lin, Harnessing surface wrinkle patterns in soft matter. *Adv. Funct. Mater.* **20**, 2550–2564 (2010).
32. H. M. Whitney *et al.*, Floral iridescence, produced by diffractive optics, acts as a cue for animal pollinators. *Science* **323**, 130–133 (2009).
33. Q. Wang, M. Tahir, L. Zhang, X. Zhao, Electro-creasing instability in deformed polymers: Experiment and theory. *Soft Matter* **7**, 6583–6589 (2011).
34. S. M. Kang *et al.*, Directional oil sliding surfaces with hierarchical anisotropic groove microstructures. *Adv. Mater.* **25**, 5756–5761 (2013).
35. J. Cha, H. Shin, P. Kim, Crack/fold hybrid structure-based fluidic networks inspired by the epidermis of desert lizards. *ACS Appl. Mater. Interfaces* **8**, 28418–28423 (2016).
36. Q. Guo *et al.*, A cephalopod-inspired mechanoluminescence material with skin-like self-healing and sensing properties. *Mater. Horiz.* **6**, 996–1004 (2019).
37. B. Jiang *et al.*, Fast dual-stimuli-responsive dynamic surface wrinkles with high bistability for smart windows and rewritable optical displays. *ACS Appl. Mater. Interfaces* **11**, 40406–40415 (2019).
38. B. Jiang, L. Liu, Z. Gao, W. Wang, A general and robust strategy for fabricating mechanoresponsive surface wrinkles with dynamic switchable transmittance. *Adv. Opt. Mater.* **6**, 1800195 (2018).
39. M. S. Zafar *et al.*, "Bioactive surface coatings for enhancing osseointegration of dental implants" in *Biomedical, Therapeutic and Clinical Applications of Bioactive Glasses*, G. Kaur, Ed. (Woodhead Publishing, 2019), pp. 313–329.
40. K. Yue, J. Nan, X. Zhang, J. Tang, X. Zhang, Photothermal effects of gold nanoparticles induced by light emitting diodes. *Appl. Therm. Eng.* **99**, 1093–1100 (2016).
41. G. S. Terentyuk *et al.*, Photothermal effects induced by laser heating of gold nanorods in suspensions and inoculated tumours during in vivo experiments. *Quantum Electron.* **42**, 380 (2012).
42. R. Ghaemi *et al.*, Use of flame activation of surfaces to bond PDMS to variety of substrates for fabrication of multimaterial microchannels. *J. Micromech. Microeng.* **28**, 087001 (2018).
43. S. Farris *et al.*, The fundamentals of flame treatment for the surface activation of polyolefin polymers: A review. *Polymer (Guildf.)* **51**, 3591–3605 (2010).
44. B. Osmani *et al.*, *Morphology and Conductivity of Au Films on Polydimethylsiloxane Using (3-Mercaptopropyl)Trimethoxysilane (MPTMS) as an Adhesion Promoter, SPIE Smart Structures and Materials + Nondestructive Evaluation and Health Monitoring* (SPIE, 2016), **vol. 9798**.
45. I. Byun, A. W. Coleman, B. Kim, Transfer of thin Au films to polydimethylsiloxane (PDMS) with reliable bonding using (3-mercaptopropyl) trimethoxysilane (MPTMS) as a molecular adhesive. *J. Micromech. Microeng.* **23**, 085016 (2013).
46. K. J. Lee, K. A. Fosser, R. G. Nuzzo, Fabrication of stable metallic patterns embedded in poly(dimethylsiloxane) and model applications in non-planar electronic and lab-on-a-chip device patterning. *Adv. Funct. Mater.* **15**, 557–566 (2005).
47. K. Efimenko, W. E. Wallace, J. Genzer, Surface modification of Sylgard-184 poly(dimethyl siloxane) networks by ultraviolet and ultraviolet/ozone treatment. *J. Colloid Interface Sci.* **254**, 306–315 (2002).
48. T. Ohzono, K. Suzuki, T. Yamaguchi, N. Fukuda, Tunable optical diffuser based on deformable wrinkles. *Adv. Opt. Mater.* **1**, 374–380 (2013).
49. I. D. Johnston, D. K. McCluskey, C. K. L. Tan, M. C. Tracey, Mechanical characterization of bulk Sylgard 184 for microfluidics and microengineering. *J. Micromech. Microeng.* **24**, 035017 (2014).
50. F. Schneider, T. Fellner, J. Wilde, U. Wallrabe, Mechanical properties of silicones for MEMS. *J. Micromech. Microeng.* **18**, 065008 (2008).
51. S. Nikravesh, D. Ryu, Y.-L. Shen, Direct numerical simulation of buckling instability of thin films on a compliant substrate. *Adv. Mech. Eng.* **11**, 1687814019840470 (2019).
52. S. Nikravesh, D. Ryu, Y.-L. Shen, Instabilities of thin films on a compliant substrate: Direct numerical simulations from surface wrinkling to global buckling. *Sci. Rep.* **10**, 5728 (2020).
53. S. Nikravesh, D. Ryu, Y.-L. Shen, Surface instability of composite thin films on compliant substrates: Direct simulation approach. *Front. Mater.* **6**, 214 (2019).
54. H. Chi, Y. J. Liu, F. Wang, C. He, Highly sensitive and fast response colorimetric humidity sensors based on graphene oxides film. *ACS Appl. Mater. Interfaces* **7**, 19882–19886 (2015).
55. Y. Fu, C. A. Tippets, E. U. Donev, R. Lopez, Structural colors: From natural to artificial systems. *Wiley Interdiscip. Rev. Nanomed. Nanobiotechnol.* **8**, 758–775 (2016).
56. C.-C. Fu *et al.*, Tunable nanowrinkles on shape memory polymer sheets. *Adv. Mater.* **21**, 4472–4476 (2009).